PCCP

ROYAL SOCIETY OF CHEMISTRY

PAPER

View Article Online
View Journal | View Issue

Cite this: *Phys. Chem. Chem. Phys.*, 2026, **28**, 79

W-incorporated high-performance layered cathode materials for advanced lithium-ion batteries

Xiaoyi Hou,* Haozhe Wu, Qirongxin Shen, Dengdeng Ai and Xi Wu

Received 5th September 2025,
Accepted 9th November 2025

DOI: 10.1039/d5cp03428k

rsc.li/pccp

High-nickel cobalt-free cathode materials are regarded as some of the promising candidates for high-energy-density lithium-ion batteries due to their excellent attributes of high capacity and cost-effectiveness. However, increasing the nickel content and removing cobalt lead to degradation of the electrode–electrolyte interfacial environment and other bulk-phase layered structure issues, which significantly compromise the battery's cycle life. In this work, a W-doped $LiNi_{0.90}Mn_{0.07}Al_{0.03}O_2$ cathode material was synthesized by introducing a small amount (2 mol%) of tungsten (W) during the lithiation procedure. The W-doping enhanced the cyclic stability of the $LiNi_{0.90}Mn_{0.07}Al_{0.03}O_2$ cathode (capacity retention after 100 cycles: 90.82% *vs.* 88.99% for the pristine material at 4.3 V) remarkably. These improvements are attributed to the high-valence W^{6+} passivating the cathode material surface activity, thereby stabilizing the bulk structure and electrode–electrolyte interface. These findings provide valuable strategic insights for developing high-nickel, cobalt-free cathode materials in lithium-ion batteries.

1. Introduction

Due to the high operating voltage, low production cost, and superior reversible capacity, high-nickel ternary layered cathode materials ($LiNi_xCo_yMn_{1-x-y}O_2$, $LiNi_xCo_yAl_{1-x-y}O_2$, $x \geq 0.6$) have been widely used in new energy vehicles, electric bicycles, and smart wearable devices.[1–5] Extensive studies have demonstrated that the specific capacity of the layered cathode materials exhibits a positive relationship with the nickel content. Consequently, ultrahigh-nickel (Ni $\geq$ 0.9) layered oxides have emerged as a predominant research focus to achieve considerable energy density ($>$220 mAh g^{-1}).[6–8] Simultaneously, the continuously rising cobalt price, driven by geopolitical instability and inherent resource scarcity in main production regions, has accelerated the development of cobalt-free cathode materials. This strategic shift, however, introduces significant challenges: the absence of cobalt not only degrades electronic conductivity and reaction kinetics due to the loss of the Co^{3+}/Co^{4+} conductive pathway but also exacerbates structural collapse and cation mixing by weakening the Co–O bond stability, while simultaneously compromising thermal stability and introducing greater safety risks.[9] Consequently, the combination of ultra-high nickel content and cobalt absence generally delivers adverse effects on the overall electrochemical performance.[10,11]

In such cobalt-free systems, the inherent issues of ultra-high nickel content are further aggravated. The ultra-high nickel content inevitably causes unstable Ni^{4+} species during deep charge/discharge cycles. These metastable Ni^{4+} ions are reduced to the stable Ni^{2+} ions through parasitic reactions with electrolytes.[12–16] This process triggers severe interfacial side reactions and leads to excessive cathode electrolyte interphase (CEI) growth. Furthermore, the accumulated Ni^{2+} ions (ionic radius: 0.69 Å) preferentially migrate into Li layers (Li^+ = 0.76 Å) due to their similar ionic radii and exacerbate cation disorder.[17] This structural defect hinders the transmission of lithium ions as well as the reversible intercalation/de-intercalation reaction, deteriorating rate capability and cycling stability.[18,19]

To address these inherent challenges of high-nickel layered cathode materials, researchers have developed comprehensive modification strategies including ion doping,[20] surface coating,[21] core–shell architecture,[22] and concentration gradient design.[23,24] Based on the above discussions, strategies such as multifunctionalization,[25] interface engineering,[26] and all-solid-state thin-film microbatteries[27,28] have been proposed for battery systems. Among these approaches, ion doping emerges as the most straightforward and effective method for mitigating Li^+/Ni^{2+} cation mixing and stabilizing the layered structure.[29,30] The doping mechanism involves incorporating elements into the crystal lattice to form the robust transition metal–oxygen bonds (TM–O) and expand the interlayer spacing, which could suppress lattice oxygen release and transition metal dissolution during deep cycling.[31,32] Different dopants occupy specific

Physics and Electronic Information Engineering, Qinghai Normal University, Xining, 810008, China

crystallographic sites according to their ionic characteristics, with high-valence cations (W^{6+}, Al^{3+}, Zr^{4+}, and Ta^{5+})[33–36] preferentially substituting transition metal sites to enhance structural integrity, anions (F^- and Cl^-)[37,38] stabilizing the oxygen sublattice, and divalent cations (Mg^{2+} and Zn^{2+})[39,40] occupying lithium sites to block Ni^{2+} migration. Notably, W^{6+} doping demonstrates exceptional effectiveness due to its high valence state that facilitates charge compensation while simultaneously modifying the microstructure to inhibit microcrack formation and strengthen interfacial stability through the formation of a thin protective CEI layer. These multifunctional improvements collectively enhance the structural, thermal, and electrochemical stability of the cathode material, with W^{6+}-doped systems exhibiting superior performance in suppressing cation disorder and maintaining capacity retention during high-rate cycling. Building upon these findings, researchers Zhao *et al.*[41] successfully synthesized a 1 mol% W^{6+}-doped NCW-2 cathode material using WO_3 as the tungsten source and $Ni_{0.9}Co_{0.1}(OH)_2$ as the precursor through high-energy ball milling. The resulting NCA-2 cathode demonstrated exceptional electrochemical performance, delivering an initial discharge capacity of 204.44 mAh g^{-1} at 1C with 93.25% capacity retention after 100 cycles. In a parallel development, researchers Yang *et al.*[42] employed a solid-state reaction method with LiOH, NiO, Co_3O_4, MnO_2, Al_2O_3, and WO_3 precursors to fabricate $LiNi_{0.895}Co_{0.04}Mn_{0.03}Al_{0.03}W_{0.005}O_2$ (W-NCMA), which achieved 95% capacity retention after 100 cycles at 0.5C. While these studies conclusively demonstrate W^{6+} doping efficacy in Co-containing high-nickel cathodes, the research landscape remains notably sparse regarding its application in cobalt-free systems. This gap underscores the critical need for systematic investigation of W^{6+} doping effects in high-nickel cobalt-free layered cathodes to establish comprehensive structure–property relationships.

In this study, we synthesized $LiNi_{0.90}Mn_{0.07}Al_{0.03}O_2$ (NMA) cathode materials with varying W^{6+} doping concentrations (0–0.03 mol) using $Ni_{0.90}Mn_{0.07}Al_{0.03}(OH)_2$ as the precursor and WO_3 as the dopant source. Systematic characterization revealed that the optimal 0.02 mol W^{6+} doping concentration effectively suppressed secondary particle growth, creating shorter Li^+ diffusion pathways that significantly enhanced rate capability. The refined microstructure simultaneously provided increased electroactive surface area for improved reaction kinetics, ultimately delivering exceptional cycling stability with 90.82% capacity retention after 100 cycles at 1C under high current density conditions.

2. Experimental section

2.1. Materials preparation

2.1.1. Synthesis of the $Ni_{0.90}Mn_{0.07}Al_{0.03}(OH)_2$ precursor. The spherical $Ni_{0.90}Mn_{0.07}Al_{0.03}(OH)_2$ precursor was synthesized *via* a coprecipitation method. 1 L of deionized water was introduced into a three-neck flask equipped with a constant-temperature heating mantle and maintained under a continuous nitrogen flow (500 rpm stirring) while being gradually heated to 60 °C. Stoichiometric amounts of $Ni(NO_3)_2{\cdot}6H_2O$ (Aladdin, analytical reagent grade, 99.9%), $MnSO_4{\cdot}H_2O$ (Aladdin, analytical reagent grade, 99.9%), and $Al(NO_3)_3{\cdot}9H_2O$ (Aladdin, analytical reagent grade, 99.9%) (90 : 7 : 3 molar ratio) were precisely weighed and dissolved with moderation PEG 6000 and PEG 200 to form a homogeneous mixed metal solution (0.05 mol L^{-1} total concentration). The temperature was then elevated to 83 °C under constant stirring.

For the precipitation reaction, di-*n*-butylamine ($C_8H_{19}N$, Aladdin, analytical reagent grade) was added dropwise at a controlled rate when the temperature stabilized at 83 °C. The reaction proceeded for 5 h under isothermal conditions (83 ± 1 °C) with persistent nitrogen flow to ensure an oxygen-free environment. The resulting mixed hydroxide suspension was aged for 12 h under static conditions, followed by filtration, washing with deionized water, and vacuum drying at 80 °C for 12 h to obtain the precursor.

2.1.2. Preparation of W^{6+}-doped Li $Ni_{0.90}Mn_{0.07}Al_{0.03}O_2$ cathodes. The $Ni_{0.90}Mn_{0.07}Al_{0.03}(OH)_2$ precursor was mixed with $LiOH{\cdot}H_2O$ (Aladdin, analytical reagent grade, 99.99%) and WO_3 (Aladdin, analytical reagent grade, 99.9%) according to their molar ratios of 1 : 1.04 : *x* (where *x* represents 0, 0.01, 0.02, and 0.03 molar ratios of W doping). The precisely weighed components were homogenized *via* planetary ball milling (zirconia media, 500 rpm, 2 h) to ensure a homogeneous distribution. The mixed powder was loaded into a tube furnace under flowing oxygen atmosphere (100 mL min^{-1}) and subjected to a controlled thermal treatment protocol: first heated to 500 °C at 5 °C min^{-1} and maintained for 5 h, subsequently raised to 750 °C at 5 °C min^{-1} and maintained for 20 h, followed by naturally cooling to room temperature, yielding W^{6+}-doped $LiNi_{0.90}Mn_{0.07}Al_{0.03}O_2$ cathode materials. The resulting products were designated as NMA (undoped), W-0.01 (1 mol% W), W-0.02 (2 mol%), and W-0.03 (3 mol%) based on their nominal tungsten content.

2.2. Material characterization

The crystal structure of the cathode material was characterized by powder X-ray diffraction (XRD) using a SmartLab diffractometer (Rigaku, Japan) with Cu Kα radiation operated at 40 kV and 150 mA. Data were collected over a 2θ range of 10–80° with a scan rate of 10° min^{-1}. The morphology of the cathode material was observed using scanning electron microscopy (SEM, Zeiss Sigma 300) and transmission electron microscopy (TEM, Thermo Scientific Talos F200i S/TEM, 200 kV). High-resolution TEM imaging was performed for lattice spacing analysis. The surface elemental composition of the cathode material was analyzed by X-ray photoelectron spectroscopy (XPS; Thermo Fisher Scientific K-Alpha). All binding energies were calibrated using the C 1s peak at 284.8 eV as a reference.

2.3. Electrochemical characterization

The cathode material, conductive carbon black, and polyvinylidene fluoride (PVDF) were homogeneously mixed in a weight ratio of 8 : 1 : 1 in a beaker. *N*-Methyl-2-pyrrolidone (NMP) was added dropwise under stirring until a uniform mixture was

formed. Magnetic stirring was applied at 450 rpm for 4 h. The slurry was coated onto aluminum foil and vacuum-dried at 80 °C for 12 h. The dried electrodes were roll-pressed and cut into 16-mm-diameter disks. For electrochemical testing, coin-type half-cells (CR2032) were assembled in an argon-filled glove box (< 0.01 ppm H_2O/O_2) using 1 M $LiPF_6$ in ethylene carbonate (EC)/diethyl carbonate (DEC)/dimethyl carbonate (DMC) (1 : 1 : 1 by volume) as the electrolyte and lithium metal as the counter electrode. Charge/discharge tests were performed in constant-current mode on a Neware system (CT-4008T-5V6A, China) at 2.5–4.3 V and 25 °C. Rate capability was evaluated at 0.1–5C (1C = 180 mA g^{-1}). Cyclic voltammetry (CV) was conducted at 0.1 mV s^{-1} (2.5–4.3 V) using a CHI660e workstation. Electrochemical impedance spectroscopy (EIS) measurements were performed from 0.01 Hz to 100 kHz with a 10 mV amplitude. All tests were maintained at room temperature (25 °C).

3. Results and discussion

The synthesized cathode materials were characterized by X-ray diffraction (XRD) to investigate the evolution of their diffraction peaks. As shown in Fig. 1a, the W^{6+}-modified W-0.01, W-0.02 and W-0.03 samples exhibit similar diffraction patterns to the pristine NMA, all demonstrating a typical α-$NaFeO_2$ hexagonal layered structure with the $R\bar{3}m$ space group, which matches well with the standard PDF card (PDF #09-0063).[43,44] This indicates that W^{6+} doping does not introduce any impurity phases in the cathode materials. As shown in Fig. 1b and c, the clear splitting of the (006)/(012) and (011)/(018) peak doublets further confirms that all four cathode materials maintain well-ordered layered structures.[45]

To systematically investigate the effects of varying W^{6+} doping concentrations on structural parameters, Rietveld refinement of XRD patterns was performed using Fullprof software, with refinement profiles shown in Fig. 1d–g (panels d–g corresponding to NMA, W-0.01, W-0.02, and W-0.03, respectively). As summarized in Table 1, all refined patterns exhibit satisfactory reliability factors (R_p and R_{wp} < 10%), confirming the credibility of refinement results.

The refinement data reveal a gradual expansion along the *c*-axis with increasing W^{6+} content. This anisotropic lattice expansion is attributed to the larger ionic radius of W^{6+} (0.60 Å) compared to Ni^{3+} (0.56 Å).[46] Since the *c*-axis corresponds to the (003) crystallographic plane, this expansion indicates that W^{6+} doping effectively enlarges the interplanar spacing, which is expected to provide wider Li^+ diffusion channels and could potentially enhance the rate capability.

Notably, the refined unit cell volumes (*V*) demonstrate a non-monotonic variation trend – initially decreasing then increasing with W content – suggesting that the 0.02 mol W^{6+} doping optimally suppresses grain growth through solid-solution strengthening effects induced by W^{6+} incorporation. The *c*/*a* ratios, critical indicators of layered structure integrity, maintain values exceeding 4.9 for all samples (NMA and W-doped variants), unambiguously confirming their well-ordered layered configurations.[47,48]

Complementary to the structural parameters, the cation mixing behavior was quantitatively analyzed through XRD refinement. The results reveal a non-monotonic variation in Li^+/Ni^{2+} cation mixing with increasing W^{6+} doping content, showing an initial decrease followed by an increase compared to the pristine material. Fundamentally, this phenomenon originates from charge compensation effects – as excessive incorporation (> 0.02 mol) of a high-valence cation (W^{6+}) inevitably induces the reduction of Ni^{3+} to Ni^{2+} to maintain charge balance, thereby promoting Li^+/Ni^{2+} mixing.[49–51]

Among all doped cathodes, the 0.02 mol W^{6+}-modified sample exhibits optimal electrochemical performance, demonstrating both the minimal cation mixing degree (2.63%) and the highest $I_{(003)}/I_{(104)}$ intensity ratio (1.727), which collectively indicate superior structural ordering and reduced Li^+/Ni^{2+} disorder compared to other doping concentrations.[52] These values are superior to both the pristine material and other doping concentrations (Table 1), providing compelling evidence that appropriate W^{6+} doping can effectively minimize Li^+/Ni^{2+} cation disorder in layered cathode materials.

The morphological characteristics of four cathode materials (pristine NMA, W-0.01, W-0.02, and W-0.03) were systematically investigated through scanning electron microscopy (SEM) to elucidate the influence of varying W^{6+} doping concentrations on their morphological evolution, as shown in Fig. 2a–d. All samples remain largely unchanged, with the materials retaining a spherical shape resulting from the compact stacking of primary particles. Moreover, with increasing W^{6+} content, the secondary particle size demonstrates an initial decrease followed by an increase, a phenomenon that confirms that an appropriate amount of W^{6+} can modify the primary particle size.

The particle size plays a pivotal role in influencing the electrochemical performance as a larger specific surface area and smaller particle size facilitate lithium ion transport.[53] The W-0.02 sample exhibits the smallest particle size, which may positively influence the Li-ion diffusion kinetics. To further investigate the microstructure, higher-magnification observations reveal that W-0.02 exhibits more densely packed primary particles and a smoother surface morphology (Fig. 2e–h). This clearly demonstrates that W^{6+} doping effectively regulates the microstructural evolution, leading to compact secondary particles. The enhanced particle compactness and reduced size in W-0.02 not only reinforce the crystal structure integrity but also increase the specific surface area, providing abundant electrochemically active sites that ultimately maximize the performance of this high-nickel layered cathode material. As evidenced by TEM and corresponding FFT patterns (Fig. 2i and j), both pristine NMA and W-0.02 exhibit well-defined (003) crystallographic planes, confirming layered structure preservation and the absence of W^{6+} induced impurities. IFFT analysis further reveals interlayer spacing expansion from 0.490 nm to 0.493 nm upon doping, attributed to a larger ionic radius of W. This lattice expansion facilitates Li^+ migration

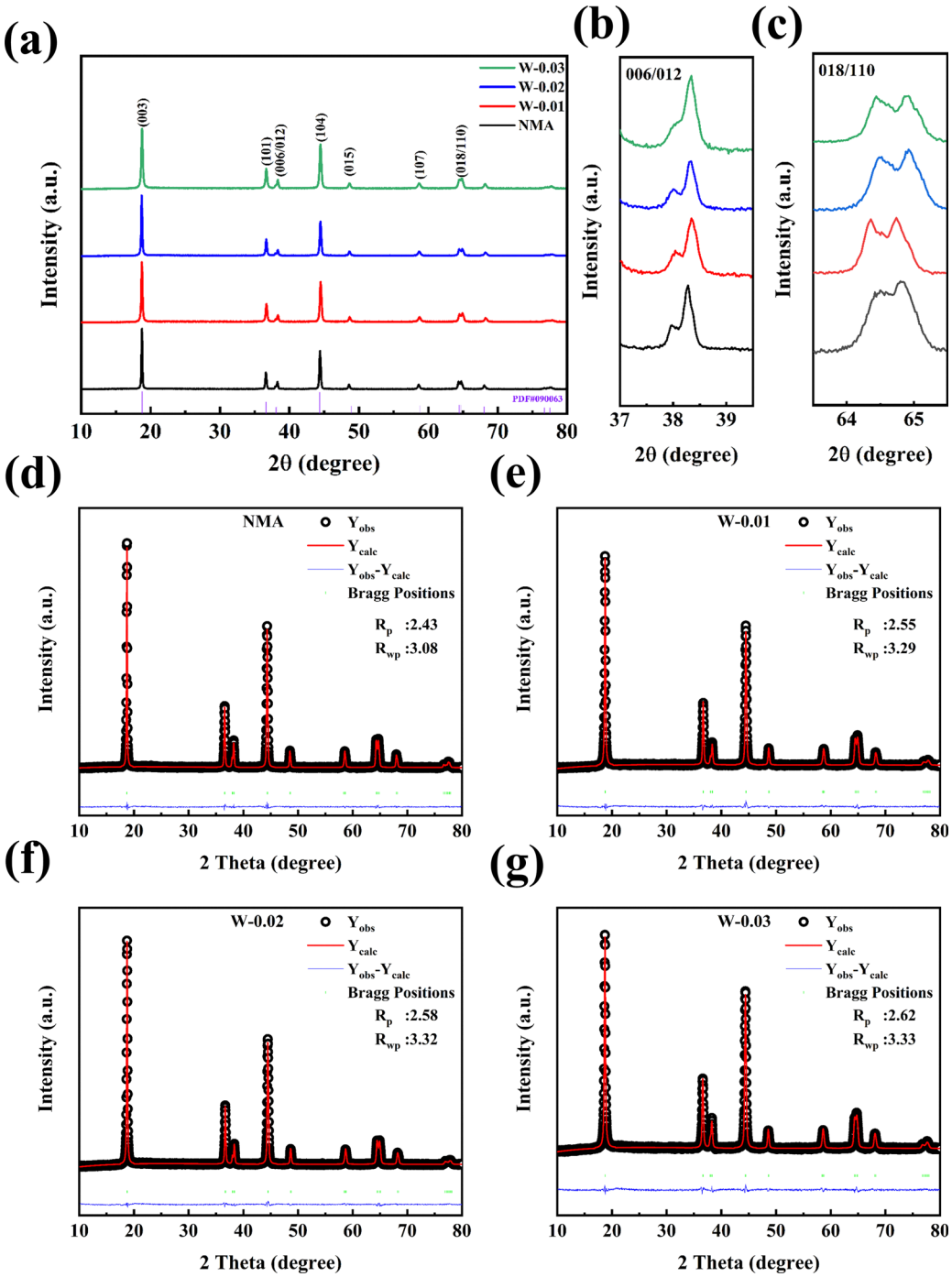

Fig. 1 (a) XRD patterns of pristine NMA and W^{6+}-doped samples (W-0.01, W-0.02, W-0.03); magnified view of the (b) (006)/(012), and (d) (011)/(018) peak doublets; Rietveld refinement results of the XRD patterns for (d) pristine NMA, (e) W-0.01, (f) W-0.02, and (g) W-0.03 samples.

Table 1 Rietveld refinement parameters of XRD patterns for pristine NMA and W^{6+}-doped $LiNi_{0.90}Mn_{0.07}Al_{0.03}O_2$ cathodes

	a (Å)	c (Å)	V (Å^3)	c/a	$I_{(003)}/I_{(104)}$	Li^+/Ni^{2+} (%)	R_p (%)	R_{wp} (%)
NMA	2.8791	14.1984	102.100	4.931	1.548	4.72	2.43	3.08
W-0.01	2.8705	14.1944	101.599	4.945	1.462	4.02	2.55	3.29
W-0.02	2.8709	14.1980	101.344	4.945	1.727	2.63	2.58	3.32
W-0.03	2.8762	14.2120	101.822	4.941	1.327	3.97	2.62	3.33

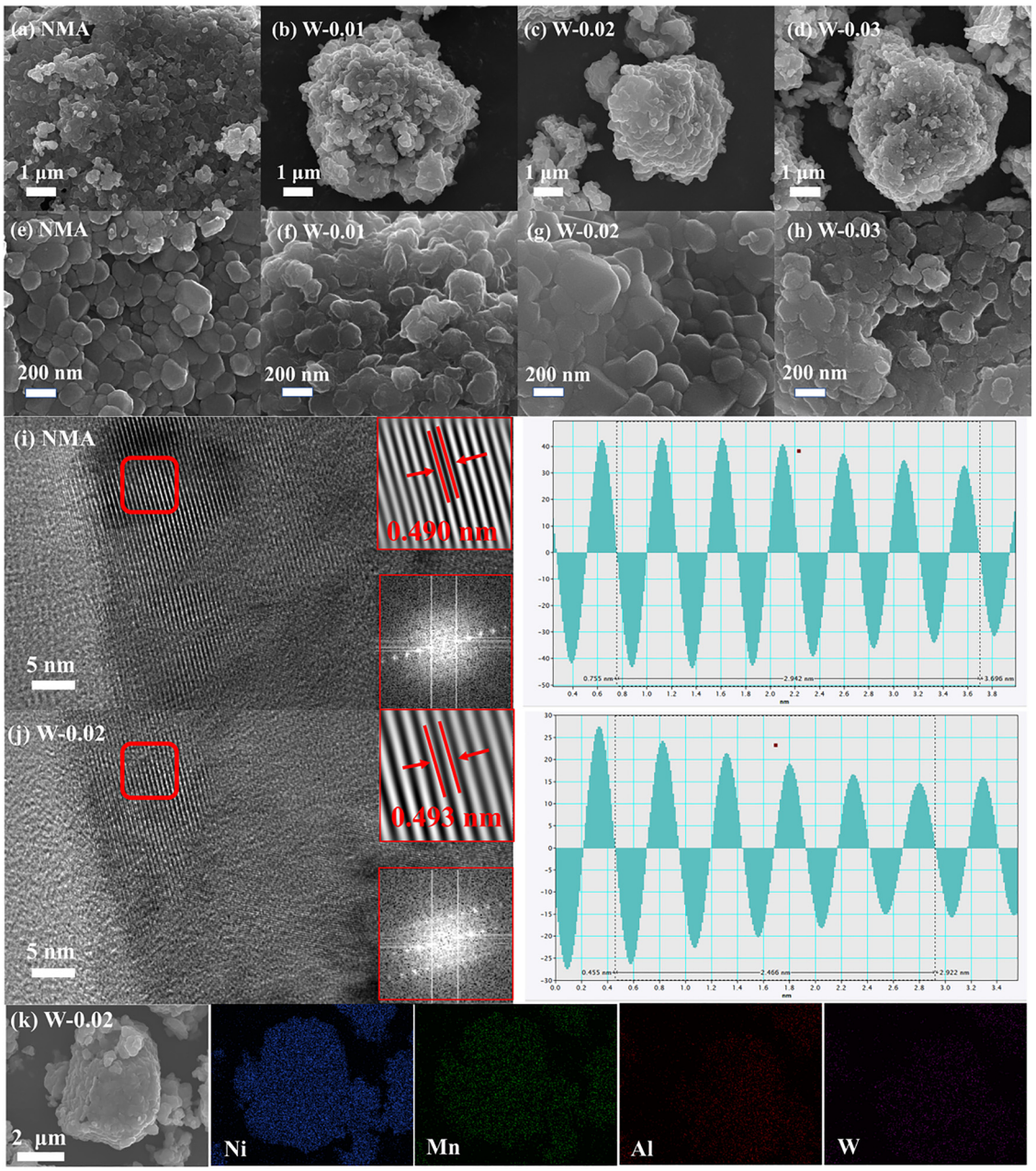

Fig. 2 Morphological and structural characterization of pristine and W^{6+}-doped $LiNi_{0.90}Mn_{0.07}Al_{0.03}O_2$ cathodes: (a–d) SEM images showing secondary particle morphology of (a) NMA, (b) W-0.01, (c) W-0.02, and (d) W-0.03; (e–h) Corresponding high-magnification SEM images revealing primary particle arrangements; (i) TEM image of NMA displaying lattice fringes with inset fast Fourier transform (FFT) pattern; (j) TEM image of W-0.02 with corresponding FFT pattern (inset) demonstrating improved crystallinity; (k) EDS elemental mapping of W-0.02 confirming homogeneous distribution of Al (red), Ni (blue), Mn (green), and W (purple) throughout secondary particles.

while alleviating volumetric variations during charge/discharge processes.[54,55]

Finally, EDS analysis confirms successful W doping with uniform distribution in both bulk and surface regions (Fig. 2k), as evidenced by the co-existence of Ni, Mn, Al, and W signals.

X-ray photoelectron spectroscopy (XPS) was employed to characterize the valence states of W and Ni in the cathode materials, and shown in Fig. 3. As expected, pristine NMA shows no detectable W signals (Fig. 3a). The W $4f_{5/2}$ and W $4f_{7/2}$ doublet peaks are clearly observed in W-0.02, confirming the successful incorporation of W^{6+} at the 0.02 mol doping level. Identical W 4f spectral features were observed in W-0.01 and W-0.03 samples (Fig. 3b). This demonstrates that the W 4f characteristic peaks can be detected in samples with different tungsten doping ratios. From Ni 2p spectra, the peaks at 873 and 855.2 eV are assigned to Ni $2p_{1/2}$ and Ni $2p_{3/2}$ orbitals, respectively. The Ni $2p_{3/2}$ peak can be further deconvoluted into two components at 854.6 (Ni^{2+}) and 856.0 eV (Ni^{3+})[56]

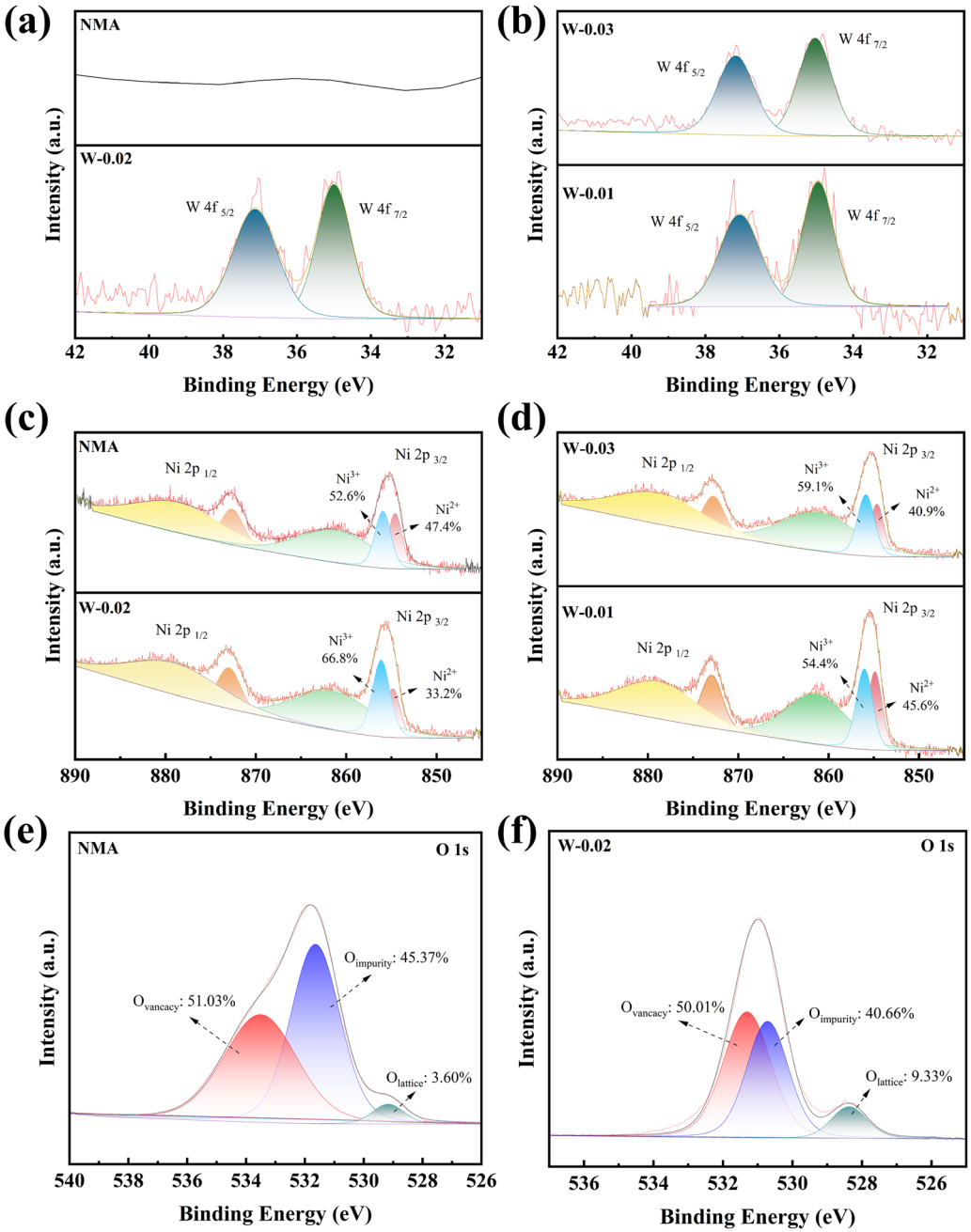

Fig. 3 The X-ray photoelectron spectroscopy (XPS) spectra of the pristine NMA and W-doped cathode materials: (a) and (b) W 4f and (c) and (d) Ni 2p orbitals across varying doping ratios; (e) and (f) O 1s orbitals of NMA and the optimal W-0.02 sample.

(Fig. 3c and d). Quantitative analysis reveals that the Ni^{3+}/Ni^{2+} ratios in the four cathodes exhibit a non-monotonic dependence on W^{6+} doping concentration, following the sequence: 1.11 (NMA), 1.20 (W-0.01), 2.00 (W-0.02), and 1.44 (W-0.03). To further probe the interfacial stability, the O 1s spectra of NMA and W-0.02 were analyzed, as shown in Fig. 3(e and f). The deconvolution results show that the oxygen impurity content in W-0.02 was 40.66%, lower than that in NMA (45.37%), which indicates a reduced presence of carbonate/bicarbonate ions and suppressed interfacial side reactions. Moreover, the lattice oxygen content in W-0.02 was 9.33%, higher than that in NMA (3.60%). This collective evidence confirms that W^{6+} doping effectively inhibits the release of lattice oxygen and improves the overall interfacial stability.[57,58]

To further investigate the electrode reversibility of cathode materials, cyclic voltammetry (CV) measurements were conducted on four samples (pristine NMA, W-0.01, W-0.02, and W-0.03) between 2.5 and 4.3 V *vs.* Li/Li^+ at a scan rate of 0.2 mV s^{-1} as shown in Fig. 4a–d. All CV curves exhibit three distinct redox couples: the oxidation peaks correspond to phase transitions from hexagonal (H1) to monoclinic (M), monoclinic (M) to hexagonal (H2), and hexagonal (H2) to hexagonal (H3),

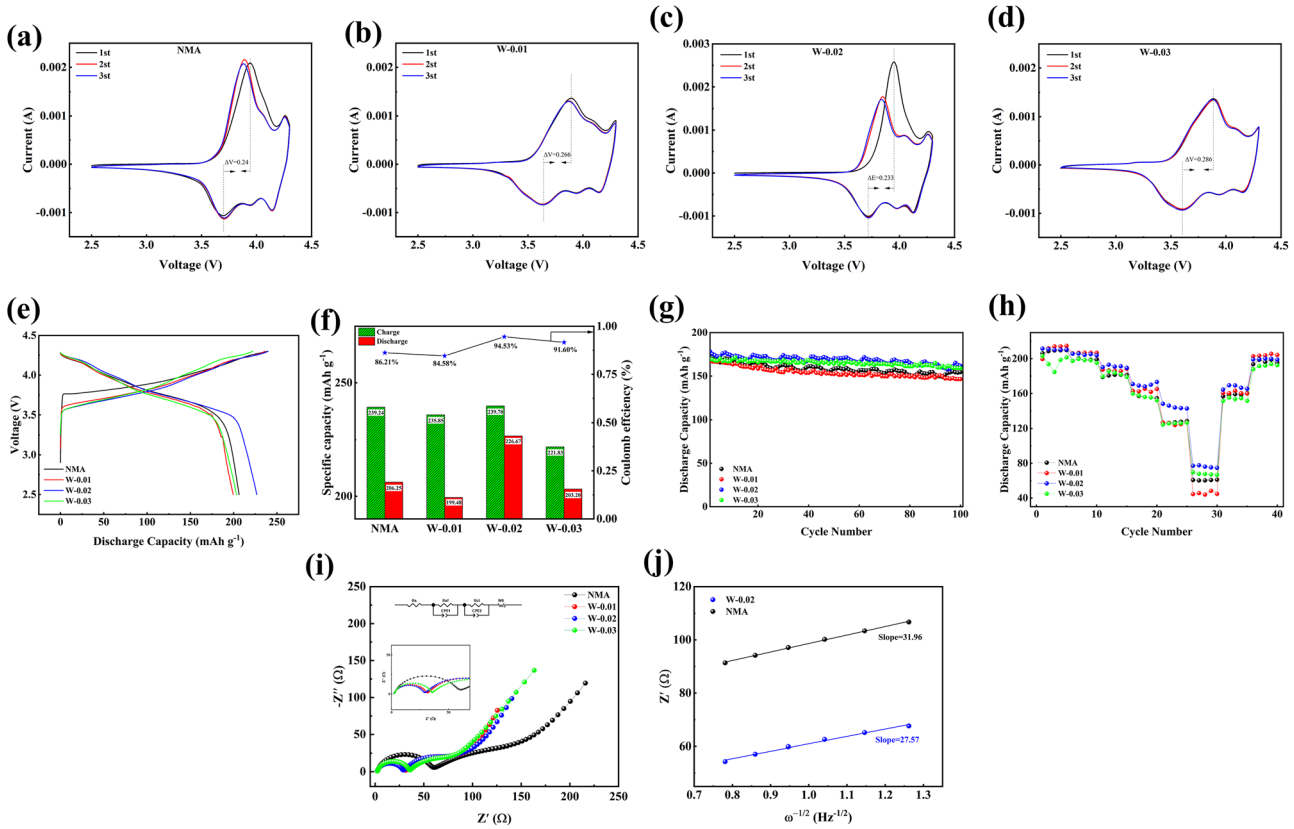

Fig. 4 Cyclic voltammetry (CV) curves of (a) NMA, (b) W-0.01, (c) W-0.02, and (d) W-0.03 cathode materials; electrochemical performance evaluation of pristine NMA and W^{6+}-doped $LiNi_{0.90}Mn_{0.07}Al_{0.03}O_2$ cathodes: (e and f) Initial charge/discharge profiles and the corresponding bar plots at 0.1C between 2.5 and 4.3 V; (g) rate capability tested at progressively increased current densities (0.1C → 5C) followed by recovery at 0.2C; (h) cycling stability at 1C over 100 cycles with Coulomb efficiency monitoring; (i) EIS plots of all cathode materials, with the equivalent circuit model shown above; (j) linear fitting plots of Z' *vs.* $\omega^{-1/2}$ for NMA and W-0.02 cathode materials.

while the reduction peaks represent the reverse transitions (H3 → H2 → M → H1).[59] The potential interval (ΔV) between the first redox couple serves as a critical indicator of electrode reversibility. NMA, W-0.01, W-0.02, and W-0.03 are 0.24, 0.266, 0.233, and 0.286 eV, respectively. Notably, W-0.02 demonstrates the smallest potential difference (0.233 eV), indicating superior electrode reversibility among all samples. This result correlates well with electrochemical performance tests, demonstrating that a small potential gap contributes to superior cycling stability by improving reaction kinetics.[60]

To investigate the effect of W^{6+} doping on electrochemical performance, coin-type CR2032 half-cells containing pristine NMA and modified samples were assembled and tested using a Neware electrochemical workstation. Fig. 4e and f displays the initial charge/discharge profiles of the cathode materials measured at 0.1C rate within a voltage window of 2.5–4.3 V. The pristine NMA, W-0.01, W-0.02, and W-0.03 samples deliver initial charge/discharge capacities of 239.24/206.25, 235.85/199.48, 239.78/226.67, and 221.83/203.20 mAh g^{-1}, respectively, with corresponding initial Coulombic efficiencies of 86.21%, 84.58%, 94.53%, and 91.60%. The high ICE is more likely due to the W-doping stabilizing the crystal structure and reducing irreversible cation mixing or phase transitions during the first cycle, thereby minimizing irreversible capacity loss.

The cycling stability of all cathode materials was further evaluated at room temperature under a current density of 1C (180 mAh g^{-1}) within a voltage window of 2.5–4.3V. As shown in Fig. 4g, the pristine NMA delivered initial and final (after 100 cycles) discharge capacities of 173.60 and 154.50 mAh g^{-1}, respectively, corresponding to a capacity retention of 88.99%. In comparison, all W-doped cathodes showed improved performance. Among them, the W-0.02 cathode exhibited the most promising combination of high capacity and cycling stability, with capacities of 178.13 and 161.78 mAh g^{-1} (90.82% retention), outperforming both W-0.01 (167.27/146.56 mAh g^{-1}, 87.62%) and W-0.03, which showed the highest retention (94.02%) but a lower initial capacity (169.13 mAh g^{-1}). Notably, although W-0.03 showed higher capacity retention, its absolute cycled capacity (159.02 mAh g^{-1}) remained lower than W-0.02, demonstrating that optimal W^{6+} doping (0.02 mol) effectively enhances high-current cycling performance.

Compared with flexible electrode systems, lithium-ion transport within the constrained crystalline framework of cathode oxides often encounters significant Li^+ diffusion limitations, resulting in relatively sluggish kinetics. Consequently, rate capability becomes a critical performance metric for practical applications of Ni-rich cathode materials. The rate performance was evaluated using half-cells cycled at 0.1C for activation,

Table 2 Impedance fitting parameters for the four cathode materials after activation

Sample	R_s (Ω)	R_{sf} (Ω)	R_{ct} (Ω)
NMA	2.22	54.29	95.15
W-0.01	2.15	27.82	28.13
W-0.02	1.96	25.55	27.40
W-0.03	2.21	32.86	45.62

followed by sequential cycling at 0.1, 0.2, 0.5, 1, 2, and 5C (5 cycles each rate), before finally returning to 0.2C as shown in Fig. 4h. The W-0.02 cathode delivered superior discharge capacities of 211.58, 205.66, 190.22, 170.80, 148.14, and 77.08 mAh g^{-1} at respective rates, maintaining 96.72% capacity recovery upon returning to 0.2C. In contrast, the pristine NMA cathode exhibited lower capacities (206.25, 197.42, 178.90, 160.12, 126.10, and 60.73 mAh g^{-1}) with only 93.88% capacity retention, demonstrating the W-0.02 sample enhanced electrochemical performance through improved Li^+ diffusion kinetics. The superior discharge capacity of W-0.01 at low current rates may be attributed to the moderate lattice expansion induced by limited W^{6+} doping, which facilitates Li^+ transport through widened diffusion channels. However, this doping level proves insufficient to stabilize the layered structure against severe structural degradation under high current densities, as evidenced by the rapid capacity fading. Conversely, the consistently inferior capacity of W-0.03 across all rates stems from excessive W^{6+} incorporation, which not only introduces redox-inactive species but also reduction in redox-active sites consequently diminishes the specific discharge capacity of the cathode material.[61]

The superior electrochemical performance of W-0.02 originates from its optimal doping concentration that simultaneously modifies the cathode morphology, reduces primary particle size, and enhances Li^+ diffusion kinetics. These structural advantages provide abundant electrochemically active sites while the strong W–O bonding stabilizes the crystal lattice, suppressing microcrack formation and reinforcing the cathode–electrolyte interphase.[62]

The impedance evolution is closely associated with interfacial stability and Li^+ transport kinetics. Thus, EIS was employed to investigate the post-activation impedance of four cathode materials, as depicted in Fig. 4i. The equivalent circuit model is illustrated alongside, with detailed fitting parameters summarized in Table 2. All four cathode materials exhibited two distinct semicircles in their Nyquist plots. The high-frequency intercept with the real axis corresponds to the ohmic resistance (R_s), representing intrinsic bulk resistance. The high-frequency semicircle originates from the solid–electrolyte interphase (SEI) film resistance (R_{sf}), formed through vigorous electrolyte oxidation/reduction reactions during initial cycling. The medium-frequency semicircle reflects the charge transfer resistance (R_{ct}), constituting the dominant component of electrochemical impedance, the slope in the low-frequency region corresponds to the Warburg impedance (σ) associated with Li^+ diffusion.[63,64]

After initial activation, the R_s values for NMA, W-0.01, W-0.02, and W-0.03 measured 2.22, 2.15, 1.96, and 2.21 Ω, respectively, demonstrating negligible variations that exclude R_s as a critical performance determinant. Notably, the R_{sf} values followed the sequence: 54.29 Ω (NMA) > 32.86 Ω (W-0.03) > 27.82 Ω (W-0.01) > 25.55 Ω (W-0.02). This is attributed to the 0.02 mol W^{6+} doping, which induces the formation of a more stable and ion-conductive interface phase in the W-0.02 cathode material. Furthermore, W-0.02 exhibited the lowest R_{ct} (27.40 Ω) among all samples after activation. Fig. 4j depicted the linear fitting of Z' *vs.* $\omega^{-1/2}$ for NMA and W-0.02 cathode materials, where the slope represents the Warburg impedance, showing an inverse linear relationship with Li^+ diffusion coefficient. A larger slope corresponds to a smaller Li^+ diffusion coefficient. The slope of W-0.02 (27.57) is lower than that of NMA (31.96), indicating faster Li^+ diffusion in W-0.02. The Li^+ diffusion coefficient (D_{Li^+}) can be calculated using the following equation:[65,66]

$$D_{Li^+} = \frac{R^2T^2}{2A^2n^4F^4C^2\sigma^2} \quad (1)$$

$$Z' = R_s + R_{ct} + \sigma\omega^{-\frac{1}{2}} \quad (2)$$

where R is the gas constant (8.314 J mol^{-1} K^{-1}), T is the absolute temperature (298.15 K), A denotes the electrode geometric area, n represents the number of transferred electrons ($n = 1$), F represents the Faraday constant ($F = 96\,485$C mol^{-1}), C is the bulk Li^+ concentration (4.99×10^{-2} mol cm^{-2}), and σ is the Warburg coefficient derived from the linear fitting of Z' *versus* $\omega^{-1/2}$. The D_{Li^+} of NMA and W-0.02 cathode materials were calculated to be 3.51×10^{-15} and 4.72×10^{-15} cm^2 s^{-1}, respectively, using the aforementioned equation. These values are consistent with the prior analysis results.

The superior electrochemical performance and enhanced Li^+ diffusion kinetics of W-0.02 compared to NMA can be attributed to (i) refined primary particle size *via* 0.02 mol W^{6+} doping facilitating Li^+ diffusion, (ii) inhibited irreversible phase transitions in the layered structure.

4. Conclusions

In summary, W^{6+}-doped $LiNi_{0.90}Mn_{0.07}Al_{0.03}O_2$ (NMA) cathode materials with controlled doping concentrations (0–0.03 mol) were successfully synthesized through a coprecipitation method combined with a high-temperature solid-state reaction using WO_3 as the tungsten precursor. Structural characterization reveals that the optimal W-0.02 effectively reduces primary particle size while enhancing structural stability, with Rietveld refinement and XPS analysis confirming significant suppression of Ni^{3+} to Ni^{2+} reduction (Ni^{3+}/Ni^{2+} ratio increasing from 1.1 to 2.0) and decreased Li^+/Ni^{2+} cation mixing from 4.72% to 2.63%. Electrochemical evaluation demonstrates outstanding performance with an initial discharge capacity of 178.13 mAh g^{-1} at 1C (2.5–4.3 V *vs.* Li^+/Li), capacity retention of 90.8% after 100 cycles (161.78 mAh g^{-1}), and 96.72%

capacity recovery when returning to 0.2C after rate testing, attributed to strengthened W–O bonding (653 kJ mol^{-1}) and optimized charge compensation. This work provides fundamental insights into cation doping strategies for high-nickel layered oxide cathodes in next-generation lithium-ion batteries.

Conflicts of interest

There are no conflicts to declare.

Data availability

All data generated or analyzed during this study are included in this published article.

Acknowledgements

This project was financially supported by the Nature Science Foundation of Qinghai (2023-ZJ-983Q).

References

1 J. Xiao, F. Shi, T. Glossmann, C. Burnett and Z. Liu, *Nat. Energy*, 2023, **8**(4), 329–339.
2 Q. Shi, F. Wu, H. Wang, Y. Lu, J. Dong, J. Zhao and L. Chen, *Energy Storage Mater.*, 2024, **67**, 103264.
3 A. Manthiram, *Nat. Commun.*, 2020, **11**(1), 1550.
4 L. Wang, T. Liu, T. Wu and J. Lu, *Nature*, 2022, **611**(7934), 61–67.
5 L. Dong, Y. Liu, K. Wen, D. Chen, D. Rao, J. Liu and W. He, *Adv. Sci.*, 2022, **9**(5), 2104699.
6 X. Ou, T. Liu, W. Zhong, X. Fan, X. Guo, X. Huang and J. Lu, *Nat. Commun.*, 2022, **13**(1), 2319.
7 Z. Tan, Y. Li, X. Xi, S. Jiang, X. Li, X. Shen and J. Zheng, *J. Energy Chem.*, 2022, **72**, 570–580.
8 K. Yang, Y. Yi, Z. Yi, C. Yang, F. Liu, K. Wang and Z. Chen, *Chem. Eng. J.*, 2023, **474**, 145554.
9 F. Wu, Q. Li, L. Chen, W. Zi, Z. R. Chen, L. Y. Bao, Y. Lu, S. Chen and Y. F. Su, *Acta Phys.-Chim. Sin.*, 2022, **38**, 2007017.
10 W. Li, E. M. Erickson and A. Manthiram, *Nat. Energy*, 2020, **5**(1), 26–34.
11 M. Li and J. Lu, *Science*, 2020, **367**(6481), 979–980.
12 Y. H. Luo, H. X. Wei, L. B. Tang, Y. D. Huang, Z. Y. Wang, Z. J. He and J. C. Zheng, *Energy Storage Mater.*, 2022, **50**, 274–307.
13 E. Hu, X. Wang, X. Yu and X. Q. Yang, *Acc. Chem. Res.*, 2022, **51**(2), 290–298.
14 L. De Biasi, A. Schiele, M. Roca-Ayats, G. Garcia, T. Brezesinski, P. Hartmann and J. Janek, *ChemSusChem*, 2019, **12**(10), 2240–2250.
15 Y. D. Huang, H. X. Wei, P. Y. Li, Y. H. Luo, Q. Wen, D. H. Le and J. C. Zheng, *J. Energy Chem.*, 2022, **75**, 301–309.
16 S. Vadivel, N. Phattharasupakun, J. Wutthiprom, S. Duangdangchote and M. Sawangphruk, *ACS Appl. Mater. Interfaces*, 2019, **11**(34), 30719–30727.
17 H. J. Noh, S. Youn, C. S. Yoon and Y. K. Sun, *J. Power Sources*, 2013, **233**, 121–130.
18 L. Zhang, E. A. Müller Gubler, C. W. Tai, Ł. Kondracki, H. Sommer, P. Novák and S. Trabesinger, *ACS Appl. Mater. Interfaces*, 2022, **14**(11), 13240–13249.
19 F. Wu, N. Liu, L. Chen, Y. Su, G. Tan, L. Bao and J. Tan, *Nano Energy*, 2019, **59**, 50–57.
20 Z. Sun, L. Xu, C. Dong, H. Zhang, M. Zhang, Y. Liu and Y. Chen, *J. Mater. Chem. A*, 2019, **7**(7), 3375–3383.
21 C. Sun, B. Zhao, J. Mao, K. H. Dai, Z. Y. Wang, L. B. Tang and J. C. Zheng, *Adv. Funct. Mater.*, 2023, **33**(30), 2300589.
22 Z. Wang, L. Li, H. Heo, L. Ren, Y. Wei, K. Lee and H. H. Park, *J. Colloid Interface Sci.*, 2024, **666**, 424–433.
23 H. Chen, H. Yuan, Z. Dai, S. Feng, M. Zheng, C. Zheng and Z. Wen, *Adv. Mater.*, 2024, **36**(33), 2401052.
24 J. Jeyakumar, M. Seenivasan, Y. S. Wu, S. H. Wu, J. K. Chang, R. Jose and C. C. Yang, *J. Colloid Interface Sci.*, 2023, **639**, 145–159.
25 Y. H. Xie, W. R. Zheng, J. Ao, Y. Q. Shao, X. Huang, H. Li, S. Y. Chen and X. H. Wang, *Energy Storage Mater.*, 2023, **62**, 102925.
26 J. Q. Cao, Y. H. Xie, Y. Yang, X. H. Wang, W. Y. Li, Q. L. Zhang, S. Ma, S. Y. Chen and B. G. Liu, *Adv. Sci.*, 2022, **9**(9), 2104689.
27 B. Y. Ke, S. L. Cheng, C. C. Zhang, W. Y. Li, J. Zhang, R. M. Deng, J. Lin, Q. S. Xie, B. H. Qu, L. Qiao, D. L. Peng and X. H. Wang, *Adv. Energy Mater.*, 2024, **14**(12), 2303757.
28 B. Y. Ke and X. H. Wang, *Proc. Natl. Acad. Sci. U. S. A.*, 2025, **122**(16), e2415693122.
29 M. D. Radin, S. Hy, M. Sina, C. Fang, H. Liu, J. Vinckeviciute and A. Van der Ven, *Adv. Energy Mater.*, 2017, **7**(20), 1602888.
30 B. Dong, A. D. Poletayev, J. P. Cottom, J. Castells-Gil, B. F. Spencer, C. Li and P. R. Slater, *J. Mater. Chem. A*, 2024, **12**(19), 11390–11402.
31 H. H. Ryu, K. J. Park, D. R. Yoon, A. Aishova, C. S. Yoon and Y. K. Sun, *Adv. Energy Mater.*, 2019, **9**(44), 1902698.
32 Y. Zhai, W. Yang, D. Ning, J. Yang, L. Sun, G. Schuck and X. Liu, *J. Mater. Chem. A*, 2020, **8**(10), 5234–5245.
33 H. H. Ryu, K. J. Park, D. R. Yoon, A. Aishova, C. S. Yoon and Y. K. Sun, *Adv. Energy Mater.*, 2019, **9**(44), 1902698.
34 W. Li, S. Lee and A. Manthiram, *Adv. Mater.*, 2020, **32**(33), 2002718.
35 N. Y. Park, G. Cho, S. B. Kim and Y. K. Sun, *Adv. Energy Mater.*, 2023, **13**(14), 2204291.
36 U. H. Kim, G. T. Park, B. K. Son, G. W. Nam, J. Liu, L. Y. Kuo and Y. K. Sun, *Nat. Energy*, 2020, **5**(11), 860–869.
37 B. Wang, S. Hou, Y. Zhang, Y. Zhu and T. Zhang, *J. Alloys Compd.*, 2024, **1003**, 175561.
38 L. Azhari, B. Sousa, R. Ahmed, R. Wang, Z. Yang, G. Gao and Y. Wang, *ACS Appl. Mater. Interfaces*, 2022, **14**(41), 46523–46536.
39 J. Tao, A. Mu, S. Geng, H. Xiao, L. Zhang and Q. Huang, *J. Solid State Electrochem.*, 2021, **25**(7), 1959–1974.

40 C. Xu, W. Xiang, Z. Wu, L. Qiu, Y. Ming, W. Yang and Y. Liu, *Chem. Eng. J.*, 2021, **403**, 126314.
41 S. Zhao, H. L. Ren, Y. Su, C. W. Li and X. M. Wang, *Ceram. Int.*, 2024, **50**(22), 44983–44992.
42 J. Yang, D. Gao, D. Zhang and C. Chang, *J. Energy Storage*, 2023, **63**, 107088.
43 W. Lee, S. Lee, E. Lee, M. Choi, R. Thangavel, Y. Lee and W. S. Yoon, *Energy Storage Mater.*, 2022, **44**, 441–451.
44 Y. Lei, J. Ai, S. Yang, H. Jiang, C. Lai and Q. Xu, *J. Alloys Compd.*, 2019, **797**, 421–431.
45 H. Dong, G. Liu, S. Li, S. Deng, Y. Cui, H. Liu and X. Sun, *ACS Appl. Mater. Interfaces*, 2018, **11**(2), 2500–2506.
46 C. Li, J. Liu, Y. Su, J. Dong, H. Zhan, M. Wang and L. Chen, *Energy Storage Mater.*, 2025, **74**, 103893.
47 L. Qiu, W. Xiang, W. Tian, C. L. Xu, Y. C. Li, Z. G. Wu and X. D. Guo, *Nano Energy*, 2019, **63**, 103818.
48 P. Zhou, H. Meng, Z. Zhang, C. Chen, Y. Lu, J. Cao and J. Chen, *J. Mater. Chem. A*, 2017, **5**(6), 2724–2731.
49 H. X. Wei, L. B. Tang, Y. D. Huang, Z. Y. Wang, Y. H. Luo, Z. J. He and J. C. Zheng, *Mater. Today*, 2021, **51**, 365–392.
50 Y. Lv, S. Huang, S. Lu, W. Ding, X. Yu, G. Liang and Y. Cao, *J. Power Sources*, 2022, **536**, 231510.
51 L. Shen, Y. Gu, T. Xu, Q. Zhou, P. Peng, Y. Chen and J. Zheng, *J. Colloid Interface Sci.*, 2024, **662**, 505–515.
52 A. Sati, P. Pokhriyal, A. Kumar, S. Anwar, A. Sagdeo, N. P. Lalla and P. R. Sagdeo, *J. Phys.: Condens. Matter*, 2021, **33**(16), 165403.
53 H. Kim, Y. Kong, W. M. Seong and A. Manthiram, *ACS Appl. Mater. Interfaces*, 2023, **15**(22), 26585–26592.
54 W. Li, H. Y. Asl, Q. Xie and A. Manthiram, *J. Am. Chem. Soc.*, 2019, **141**(13), 5097–5101.
55 H. H. Sun, U. H. Kim, J. H. Park, S. W. Park, D. H. Seo, A. Heller and Y. K. Sun, *Nat. Commun.*, 2021, **12**(1), 6552.
56 G. E. McGuire, G. K. Schweitzer and T. A. Carlson, *Inorg. Chem.*, 1973, **12**(10), 2450–2453.
57 Y. H. Chu, J. W. Zhou, W. X. Liu, F. L. Chu, J. H. Li and F. X. Wu, *Small Sci.*, 2023, **3**(7), 2300023.
58 W. Song, A. Gao, Y. Liu, A. Liu, H. Peng, M. Li and F. Wang, *J. Alloys Compd.*, 2025, **1010**, 177611.
59 S. Lee, C. Li and A. Manthiram, *Adv. Energy Mater.*, 2024, **14**(24), 2400662.
60 H. Shin, J. Park and W. Choi, *J. Alloys Compd.*, 2024, **988**, 174265.
61 B. Li, F. Zhang, C. Li, X. Cui, S. Li, C. Gao and N. Zhang, *J. Colloid Interface Sci.*, 2024, **672**, 776–786.
62 G. T. Park, S. M. Han, J. H. Ryu, M. C. Kim, D. H. Kim, M. S. Kim and Y. K. Sun, *ACS Energy Lett.*, 2023, **8**(9), 3784–3792.
63 A. C. Lazanas and M. I. Prodromidis, *ACS Meas. Sci. Au*, 2023, **3**(3), 162–193.
64 D. Zhang, Y. Liu, L. Wu, L. Feng, S. Jin, R. Zhang and M. Jin, *Electrochim. Acta*, 2019, **328**, 135086.
65 X. Ping, X. Pei, D. Zou, C. Wang, X. Li, C. Cao and Y. Wang, *Electrochim. Acta*, 2025, 146297.
66 H. Zhang, X. Wang, A. Naveed, T. Zeng, X. Zhang, H. Shi and Y. Liu, *Appl. Surf. Sci.*, 2022, **599**, 153933.

